Revista Internacional de Métodos Numéricos para Cálculo y Diseño en Ingeniería

Tech Science Press

https://doi.org/10.32604/rimni.2026.073667

ARTICLE

A Coupled Hydro-Mechanical Modeling Approach for Analyzing Casing Deformation in Shale Horizontal Wells under Volume Fracturing

Xianan Miao, Kangxing Dong*, Jinbo Li, Delong Yu and Zhihui Ren

School of Mechanical Science and Engineering, Northeast Petroleum University, Daqing, 163318, China

*Corresponding Author: Kangxing Dong. Email: dkx@nepu.edu.cn

Received: 23 September 2025; Accepted: 18 November 2025; Published: 06 November 2026

ABSTRACT: Horizontal-well volume fracturing has become a key stimulation technology for shale-gas development, yet casing damage during fracturing remains a critical challenge to production integrity. In this study, a fully embedded fluid–solid–damage coupled fracture-network model was developed through secondary programming within a finite-element framework, integrating hydro-mechanical coupling theory with a cohesive-zone description of rock fracture. A submodeling technique was further applied to construct a local formation-cement-casing strength model, enabling detailed simulation of casing deformation under complex, spatially varying external loads. Based on this framework, parametric analyses were performed to examine the influence of cluster spacing, horizontal stress contrast, formation elastic modulus, and injection rate on the near-wellbore stress-displacement fields. The results indicate that stress-shadow and depletion effects, along with nonuniform fracture propagation, significantly intensify stress heterogeneity around the wellbore, thereby elevating casing deformation risks. Reduced cluster spacing, lower elastic modulus, higher stress contrast, and greater injection rate collectively aggravate deformation and diminish the casing's internal-pressure capacity. These findings highlight that appropriate control of internal pressure and optimization of fracturing parameters are essential for mitigating casing damage, providing theoretical and numerical guidance for integrity management in shale-gas horizontal wells.

KEYWORDS: Horizontal well; volume fracturing; non-uniform load; casing damage; internal pressure

1 Introduction

With the continued advancement of stimulation technologies, hydraulic fracturing has grown in both scale and complexity, and casing deformation/failure induced by fracturing has become increasingly prominent. Casing damage not only leads to production loss and, in severe cases, well abandonment with substantial economic impacts [1–5], but also compromises well integrity-elevating the risks of fluid or gas leakage, groundwater contamination, and induced microseismicity. These issues have drawn joint attention from engineering practice and environmental stewardship. Field statistics report frequent casing failures worldwide: in the Marcellus shale, 32 of 62 wells exhibited failures; in the Utica shale (Canada), 28 wells were damaged after large-scale multi-stage volume fracturing [6–10]; in the Changning-Weiyuan national demonstration area (China), 32 of 90 horizontal wells experienced casing deformation. In the unconventional block investigated herein, 12 horizontal test wells were deployed; 7 wells encountered bridge-plug run-in obstruction (58.3%), and 3 wells had stage abandonments, totaling 10 discarded stages. The areal distribution of obstruction points is shown in Fig. 1. Routine stimulation could not proceed, substantially delaying

Copyright © 2027 The Authors. Published by Tech Science Press. This work is licensed under a Creative Commons Attribution 4.0 International License, which permits unrestricted use, distribution, and reproduction in any medium, provided the original work is properly cited.

development and incurring major economic losses [11–13]. Despite growing industrial concern, systematic studies on casing failure during volume fracturing remain limited.

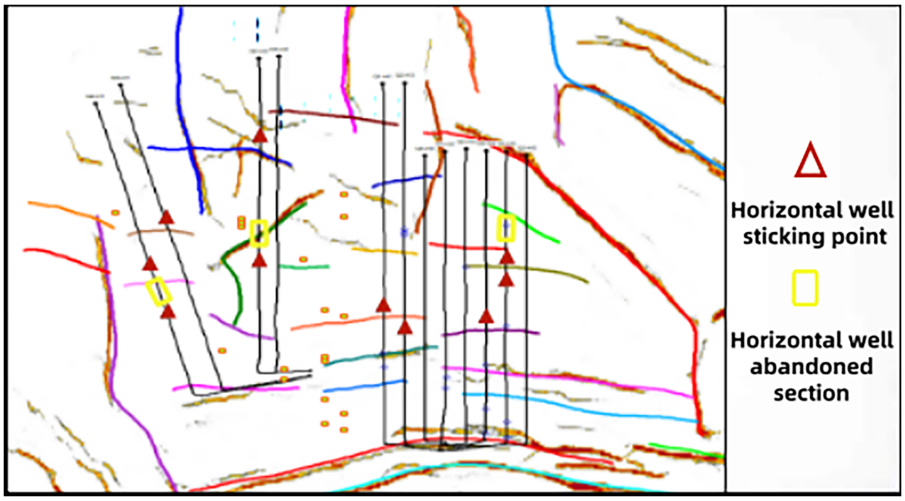


Figure 1: Plane distribution of bridge plug resistance points under the test area.

Mechanistically, casing damage during volume fracturing is mainly driven by two effects: (i) post-fracturing formation damage/weakening reduces confining support to the casing; and (ii) fracturing activates or induces shear slip along preexisting faults and natural fractures, producing highly nonuniform near-wellbore stress and displacement fields [14–16]. As the number of stages and treatment parameters evolve, the external load around the casing transitions from a simplified nonuniform surface load to a spatiotemporally complex distribution governed by multi-factor coupling [17–21]. Conventional simplified approaches, such as the commonly adopted elliptical loading model, fail to capture the actual redistribution and evolution of external loads once complex fracture networks have developed. As a result, detailed quantitative studies on casing response and failure mechanisms under nonuniform loading conditions are still limited.

In recent years, extensive research has been conducted worldwide on the mechanisms of casing deformation induced by hydraulic fracturing and on multi-field coupled modeling approaches. Recent research on casing damage during hydraulic fracturing has progressively established a multi-faceted understanding of the underlying mechanisms. Field monitoring and inversion analyses have been employed to quantify the significant influence of fracture interference on the stress distribution around the wellbore. Concurrently, hydro-mechanically coupled finite-element models have been widely adopted to simulate how these altered stress fields, particularly stress-shadow effects, lead to casing deformation. Furthermore, advanced studies integrating fracture mechanics with continuum modeling have provided deeper insights into the complex coupling between dynamic fracture propagation and the resultant nonuniform loading exerted on the casing [22–26]. These studies have provided valuable insights into stress redistribution during fracturing; however, most remain limited to two-dimensional or quasi-static assumptions and do not fully capture the dynamic interaction between fracture evolution and localized casing response. Building on this foundation, the present study develops a fully embedded fluid-solid-damage coupled model capable of simultaneously representing fracture propagation and wellbore mechanical behavior, thereby providing a more realistic depiction of stress redistribution and casing deformation mechanisms under volumetric fracturing conditions.

From a standards perspective, API specifications have long underpinned casing strength design and have been continuously refined since the 1970s [27–31]. However, under modern volume-fracturing scenarios, the external load formulations often underrepresent nonuniformity, leading to overestimation of casing capacity; prior studies indicate that nonuniform external loads may reduce casing strength to only one-third to one-sixth of traditional estimates, markedly increasing failure risk. Beyond production and safety, this gap directly affects well integrity management and environmental risk mitigation.

To address the key scientific and engineering issues related to casing damage during volume fracturing, this study develops an integrated finite element framework that couples the processes of fracturing, *in-situ* stress redistribution, and casing mechanical response. Based on rock fracture mechanics and hydro-mechanical coupling theory in porous media, a fully embedded fluid–solid–damage coupled fracture-network model is implemented within the finite element environment. By incorporating a global–local submodeling technique, the framework enables dynamic transfer of nonuniform loads induced by fracture evolution to the near-wellbore region. Unlike conventional casing deformation analyses that simplify external loads as uniform or elliptical distributions, this approach directly resolves the nonuniform stress–displacement fields generated by fracture propagation and stress perturbation, thereby capturing the realistic stress redistribution during volumetric fracturing. The model allows systematic evaluation of how key fracturing parameters affect the stress state and loading characteristics around the wellbore and introduces a strength-correction strategy for casings under nonuniform loading, providing both theoretical and numerical guidance for integrity assessment and design optimization in volume-fracturing operations.

2 Volume Fracturing Model Theory

2.1 Fluid-Structure Coupling Finite Element Theory of Porous Media

Reservoir rock is a type of porous medium consisting of a solid framework with fluid occupying the pore spaces. During volume fracturing, when fracturing fluid is injected into the formation, the permeability of the medium varies due to its interaction with the rock skeleton. The stress field will affect the pore pressure field formed by fluid migration, and the pore pressure change will in turn affect the deformation of rock skeleton. The above changes belong to a complex fluid–solid coupling mechanism. The external load of the rock mass is jointly borne by the pore fluid and the solid skeleton, and the pressure applied by the fluid in the normal direction around the pores is regarded as the pore stress. Effective stress refers to the stress transferred between the contact surfaces of the particles when the porous rock skeleton is deformed under external load.

$$\overline{\sigma} = \sigma + \left(\chi p_w + (1-\chi)\, p_a\right) I \tag{1}$$

where $\overline{\sigma}$ is effective stress in Mpa. p_w is the liquid pressure in the pore in MPa. p_a is the gas pressure in the pore in MPa. χ is a factor related to saturation, which is dimensionless and takes the value of 1 when the porous medium is fully saturated and between 0 and 1 when the porous medium is not fully saturated.

The equilibrium equation of the rock mass can be formulated on the basis of the virtual work principle, which states that, at any given moment, the virtual work performed by the external forces acting on the rock mass (including body forces and surface forces) must be equivalent to the internal virtual work within the system. This principle provides a rigorous theoretical foundation for establishing numerical models in rock mechanics, as it enables the transformation of differential equilibrium equations into a weak form that is more suitable for finite element implementation. Moreover, the use of virtual work allows for a more accurate representation of complex boundary conditions and heterogeneous material properties, which is particularly important in the analysis of crack initiation, fracture propagation, and deformation behavior

during hydraulic fracturing. Consequently, the virtual work principle not only serves as a cornerstone of computational mechanics but also plays a critical role in advancing the understanding of reservoir stability and wellbore integrity.

$$\int_V \boldsymbol{\sigma}:\delta\boldsymbol{\varepsilon} dV = \int_S \boldsymbol{t}:\delta v dS + \int_V \hat{\boldsymbol{f}} \cdot \delta v dV \tag{2}$$

where δv is the imaginary displacement field in m units. $\delta\varepsilon$ is the imaginary strain field, which is dimensionless. $\boldsymbol{\sigma}$ is the total stress in MPa. $\boldsymbol{t}$ is the surface force in units of N. $\hat{\boldsymbol{f}}$ is the volume force in units of N.

In the finite element method, the spatial discretization can be realized by Lagrange equation, and the displacement value of the element node is unknown, so the finite element can be used to simulate porous media materials, and the pore fluid flow in the rock mass can also be simulated. After dividing the formation into finite element mesh, the pore fluid flows through the mesh, and the state of pore fluid in a time increment needs to be expressed by a continuity equation. According to the fluid mass conservation equation and Darcy's law, the continuity equation of fluid is established.

The rate of change of the fluid mass inside the control volume V per unit time is given below.

$$\frac{\mathrm{d}}{\mathrm{d}t}\int_V \rho_w n_w \mathrm{d}V = \int_V \frac{1}{J}\frac{\mathrm{d}}{\mathrm{d}t}\left(J\rho_w n_w\right)\mathrm{d}V \tag{3}$$

where J is the volume ratio of the control volume before and after deformation, which is dimensionless.

The mass continuity equation of fluid can be obtained by using the mass conservation law.

$$\frac{1}{J}\frac{\mathrm{d}}{\mathrm{d}t}\left(J\rho_w n_w\right) + \frac{\partial}{\partial \boldsymbol{x}} \cdot \left(\rho_w n_w \boldsymbol{v}_w\right) = 0 \tag{4}$$

where $\boldsymbol{v}_w$ is the seepage velocity (flow velocity of fluid relative to solid skeleton) in m/s.

When the pore pressure is large and reaches the critical pressure, the fluid flows, and its flow law conforms to Darcy's law.

$$\boldsymbol{v}_w = -\frac{1}{n_w g \rho_w}\boldsymbol{k} \cdot \left(\frac{\partial p_w}{\partial \boldsymbol{x}} - \rho_w \boldsymbol{g}\right) \tag{5}$$

where $\boldsymbol{k}$ is permeability coefficient vector. $\boldsymbol{g}$ is the gravitational force acceleration vector, which is taken as 9.8 m/s.

To solve the fluid-structure interaction problem, the equilibrium equation and the seepage continuum equation must be solved simultaneously. Newton's method should be used to solve the equations. Through the finite element calculation of the above fluid mass continuity equation, the finite element scheme describing the flow of percolation fluid can be obtained. The effective stress, strain and pore pressure of the pore medium node can be solved simultaneously with the rock stress balance equation.

2.2 Crack Propagation Model

In order to avoid the issue of stress singularity encountered at the fracture tip in conventional fracture mechanics calculations, the cohesive element model is introduced to simulate both the initiation and propagation processes of cracks, which mainly involve two fundamental physical mechanisms. First, the nucleation and propagation behavior of cracks are represented according to the principles of damage mechanics. Second, the tangential fluid flow within the fracture, together with the normal filtration process, is simulated [32–35].

In this study, a bilinear cohesive damage model is adopted to characterize the initiation and progressive damage behavior of hydraulic fractures. The condition of linear elastic deformation is satisfied prior to the occurrence of initial damage. Compared with classical linear elastic fracture mechanics, this approach eliminates the need for singular stress assumptions at the crack tip, allowing a more realistic description of crack initiation and extension in heterogeneous formations. Furthermore, the cohesive model provides a unified framework to simultaneously account for mechanical fracture propagation and fluid–structure interactions, which is of great significance for analyzing fracture evolution in unconventional reservoirs. From an engineering perspective, this modeling strategy contributes to a more reliable evaluation of fracture stability, optimizes fracturing design, and offers theoretical support for improving wellbore integrity and enhancing reservoir stimulation efficiency.

$$t = \begin{Bmatrix} t_n \\ t_s \\ t_t \end{Bmatrix} = K\varepsilon = \begin{bmatrix} K_{nn} & K_{ns} & K_{nt} \\ K_{sn} & K_{ss} & K_{st} \\ K_{tn} & K_{ts} & K_{tt} \end{bmatrix} \begin{Bmatrix} \varepsilon_n \\ \varepsilon_s \\ \varepsilon_t \end{Bmatrix} \tag{6}$$

where t is the stress vector of the cohesive element. t_n, t_s and t_t are the normal and tangential stress components, respectively. K is the stiffness matrix of cohesive elements. ε is the cohesive element strain vector. ε_n, ε_s and ε_t are the normal and tangential strain components, respectively.

The quadratic nominal stress criterion is used as the judging condition for crack initiation. When the sum of the square of the ratio of the stress values in the three directions of the cohesive element and the corresponding critical stress is equal to 1, the cohesive element will be damaged.

$$\left\{\frac{\langle \sigma_n \rangle}{N_{\max}}\right\}^2 + \left\{\frac{\sigma_s}{S_{\max}}\right\}^2 + \left\{\frac{\sigma_t}{T_{\max}}\right\}^2 = 1 \tag{7}$$

where σ_{n} is the normal stress. σ_s and σ_t are shear stresses in different directions. $N_{\max}$, $S_{\max}$ and $T_{\max}$ are the critical values of normal stress and shear stress, respectively, when failure occurs.

When the cohesive unit is damaged, tensile damage or shear damage may occur on the damaged surface. The Benzeggagh-Kenane (BK) criterion is used as the criterion to judge the crack expansion in order to take into account the normal and tangential expansion of the bond element.

$$G_n^c + \left(G_s^c - G_n^c\right)\left[\frac{G_s}{G_t}\right]^{\eta} = G^c \tag{8}$$

where G_n^c, G_s^c and G_t represent the normal, first and second tangential energy release rates of the cohesive unit, respectively, in Pa·m. G_n^c and G_s^c represent the critical energy release rate of the cohesive unit in the normal and tangential directions, respectively, in Pa·m. η is a material dependent constant. G^c is the total critical energy release rate of cohesive units in mixed mode, and the unit is Pa·m.

The rate of stiffness degradation of bonding element is described by damage evolution criterion after cracking.

$$\begin{cases} t_n = \begin{cases} (1-D)\,\bar{t}_n & \bar{t}_n \geq 0 \\ \bar{t}_n & \bar{t}_n < 0 \end{cases} \\ t_s = (1-D)\,\bar{t}_s \\ t_t = (1-D)\,\bar{t}_t \end{cases} \tag{9}$$

$$D = \frac{d_m^f \left(d_m^{\max} - d_m^0\right)}{d_m^{\max}\left(d_m^f - d_m^0\right)} \tag{10}$$

where $\bar{t}_n$, $\bar{t}_s$, and $\bar{t}_t$ represent the stress state without damage in the 3 directions of the cohesive element, and the unit is Pa. t_n, t_s, and t_t represent the actual stress states of the cohesive element in 3 directions, in Pa. d_m^0 and d_m^f represent the initial damage displacement and the end damage displacement in m. $d_m^{\max}$ is the maximum displacement of the unit in m. d_m^0 and d_m^f represent the initial damage displacement and the end damage displacement in m. D represents the damage factor, the range is 0–1, D = 0 indicates no damage to the material, D = 1 indicates complete damage to the material.

When the cohesive unit produces cracks, the fluid flow in the cracks is divided into tangential flow and normal filtration, as shown in Fig. 2. The following formula is the mathematical expression of tangential flow in the fracture.

$$q = -\frac{w^3}{12\mu}\nabla p \tag{11}$$

where q represents the fluid velocity in the fracture, measured in m/s. p represents the fluid pressure in the fracture and the unit is Pa. w represents the crack width in m.

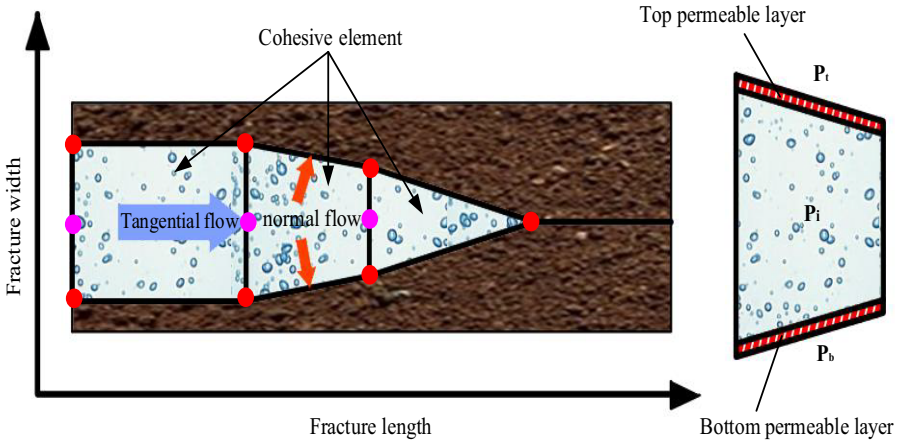


Figure 2: Schematic diagram of liquid flow in the cohesive unit.

Eqs. (3)–(11) describe the normal filtration in the fracture.

$$\begin{cases} q_t = c_t\left(p_f - p_t\right) \\ q_b = c_b\left(p_f - p_b\right) \end{cases} \tag{12}$$

where q_t and q_b represent the filtration rate of the upper and lower surfaces of the bonding unit in m/s. c_t and c_b represent the filtration coefficients of the upper and lower surfaces of the bonding unit in m/(Pa·s). p_f indicates the intermediate node pressure of the cohesive unit, and the unit is Pa. p_t and p_b represent pore pressures on the upper and lower surfaces of the cohesive unit in Pa.

3 Development of a Complex Fracture Propagation Model for Horizontal Wells

3.1 Numerical Simulation and Experimental Error Verification

According to the above theory and method, the numerical calculation model of crack propagation is established, and the simulation of casing deformation and laboratory experiment error are calculated. The finite element calculation model is shown in Fig. 3, Fig. 3a is the basic size of the simulation, and Fig. 3b is the finite element mesh model. The overall size of the model is the same as that of the true triaxial hydraulic fracturing specimen, and the length × width × height is 300 mm × 300 mm × 300 mm. There is weak bedding in the vertical direction of the model. The beam element is embedded in the formation to simulate casing in horizontal Wells, and the deformation of casing is monitored by extracting node displacement and strain at different positions of casing.

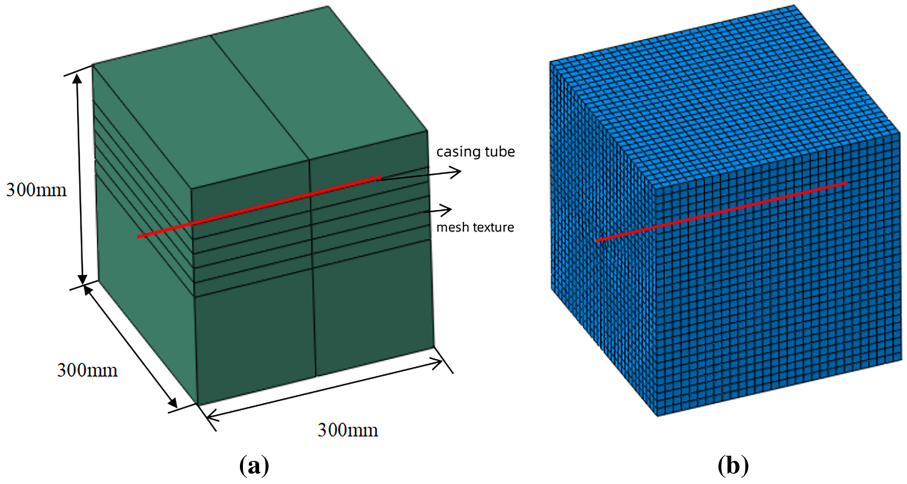
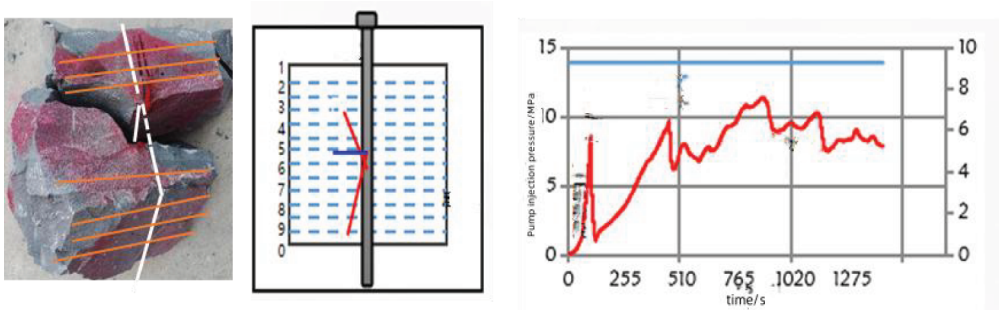


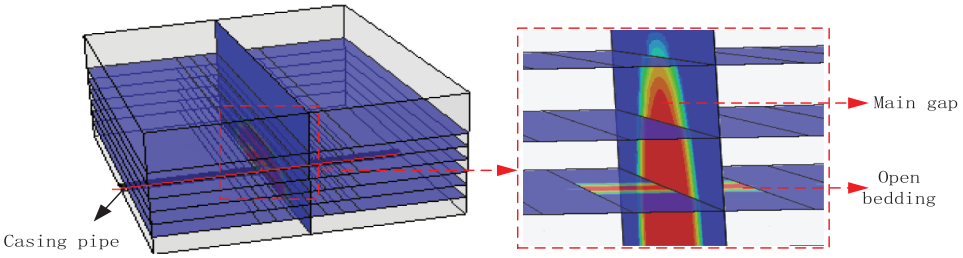
Figure 3: (a) Numerical simulation model size; (b) Finite element mesh.

The comparison between experimental and numerical fracture morphology is illustrated in Fig. 4. As shown in Fig. 4a, a primary hydraulic crack (red line in Fig. 4a) was generated in the experiment, while a bedding fracture (blue line in Fig. 4a) was also initiated. Fig. 4b further demonstrates that both a main hydraulic fracture and a bedding fracture are reproduced in the numerical simulation, and the resulting fracture propagation pattern exhibits good agreement with the experimental observations, confirming that the model can effectively simulate the cross-propagation behavior of fractures.

The stress–strain relationship of casing deformation obtained from numerical simulation was extracted and compared with that derived from experimental measurements, as illustrated in Fig. 5. The stress–strain curve obtained through simulation demonstrates a high degree of similarity to the corresponding curve from experimental testing. The numerical and experimental errors calculated at four monitoring points are provided in Table 1. As indicated in the table, the maximum deviation between the numerically simulated casing strain and the experimental results is 5%, the minimum is 1.6%, and the average error is 3.8%, which confirms that the numerical simulation approach can effectively capture the casing deformation behavior during volumetric fracturing. Validation shows that the 3D model accurately reproduces the casing stress-strain response and fracture propagation patterns observed in experiments, confirming the soundness of the model construction. A comparison between 2D and 3D simulations further indicates consistent trends and magnitudes in key response parameters, such as strain distribution and fracture initiation pressure. Therefore, the 2D model can be regarded as a simplified representation of the 3D model, suitable for large-scale engineering simulations while maintaining computational efficiency and sufficient accuracy.



(**a**) Fracture propagation and fracturing curves in physical experiment.



(**b**) Fracture propagation contour map in numerical simulation.

Figure 4: Comparative analysis of numerical and experimental fracture growth.

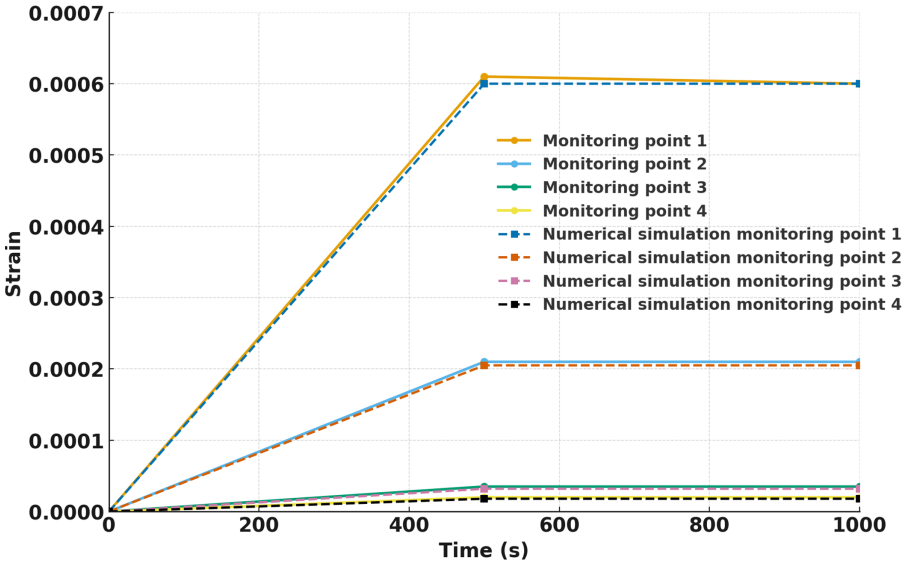


Figure 5: Comparison of stress-strain curves obtained by numerical simulation and experimental measurement.

3.2 Formation Volume Fracturing Model Development

To evaluate the nonuniform casing loads at the engineering scale, a horizontal-well volume fracturing model incorporating rock fluid–solid coupling effects was developed. The model covers an overall domain of 200 m × 200 m, with a 100 m × 100 m fracturing zone at the center where natural fractures are introduced. For simplification, the fracture spacing is set to 16 m with randomly distributed lengths. To balance engineering-scale analysis with local wellbore accuracy, a global–local submodeling approach was employed. The global model first calculates the stress and displacement fields induced by fracturing, and the resulting boundary stresses and displacements are then transferred to the formation–cement–casing

submodel. This mapping ensures continuous stress transmission and accurately captures the near-wellbore loading and casing deformation behavior.

Table 1: The levels and actual values of the design parameters.

Monitoring Point	Numerical Simulation Strain	Experimental Strain	Error
1	0.000018	0.000019	5.0%
2	0.00021	0.00022	4.5%
3	0.00061	0.00062	1.6%
4	0.000029	0.000030	3.3%

To better capture the characteristics of shale volume fracturing, an unstructured mesh was generated in the fracturing zone, as shown in Fig. 6. Cohesive elements were globally embedded within this region through secondary development using Python scripting, enabling the construction of an extended fracture network model that represents fracture initiation and propagation more realistically. In this study, the secondary finite element development was implemented within an existing FEM framework. Cohesive element generation and the fluid–solid–damage coupling module were integrated through Python scripting and user-defined subroutines, enabling the establishment of an extended fracture-network model that supports dynamic fracture propagation and fully coupled multi-physics analysis.

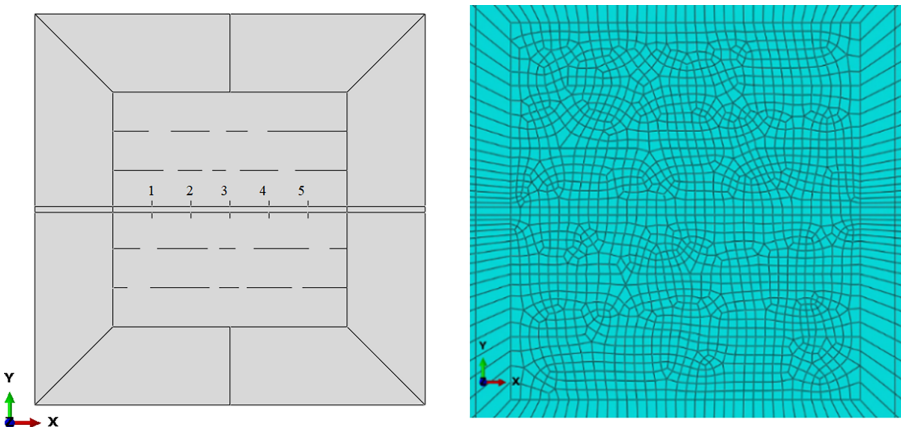


Figure 6: Formation volume fracturing model.

According to the engineering practice, a total of 5 clusters of fracturing are simulated, and the fracture growth of each cluster is represented by single fracture growth. The cohesive element CPE4P is employed to represent the reservoir pore system, while the cohesive unit type COH2D4P is adopted for fracture simulation. During the calculation procedure, the initial ground stress is introduced through the predefined module, and the coupled fluid–structure interaction in the hydraulic fracturing process is implemented and solved using the Geostatic and Soil modules. The material properties utilized in the model are presented in Table 2. The key mechanical parameters were primarily determined from triaxial compression and Brazilian splitting tests conducted on core samples from the target reservoir. Permeability, leak-off coefficient, and porosity were referenced from experimental results and published data of shale formations within the same structural zone.

Table 2: Part of the model parameters.

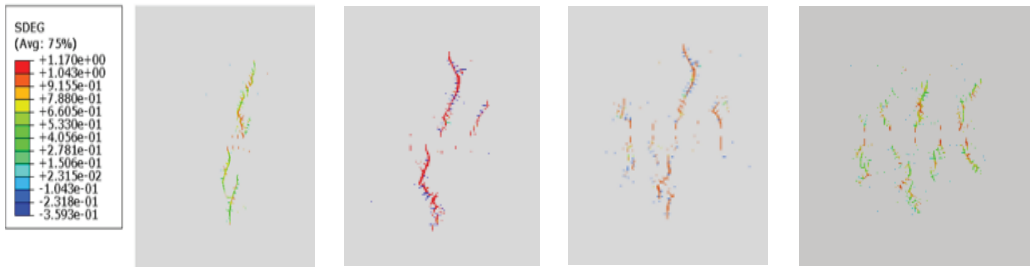
Parametert	Numerical Simulation Strain
Elastic modulus of formation (GPa)	25
Formation Poisson's ratio	0.3
Reservoir matrix tensile strength (MPa)	6
Tensile strength of bedding surface (MPa)	4
Energy of fracture (m·Pa)	3000
Coefficient of permeability (m/s)	10^{-7}
fluid loss coefficient (m/Pa·s)	10^{-13}
void ratio	0.11
Viscosity of fracturing fluid (Pa·s)	0.001

In order to elucidate the influence of formation volume fracturing on casing deformation, it is essential to investigate the stress distribution and displacement response of the rock mass adjacent to the wellbore. The present study integrates numerical simulation outcomes obtained from the established mechanical model. Two observation paths, referred to as Path 1 and Path 2, are symmetrically arranged on either side of the wellbore at a radial offset of 3 m from the borehole axis. The evolution of *in-situ* stress, strain, and deformation in the near-wellbore region following the fracturing process is extracted sequentially along the propagation of fracture stages, with specific attention given to the positive X-axis orientation of the model. Subsequently, the loading conditions acting on the casing are examined to identify the dominant factors controlling casing integrity. These results provide theoretical guidance and methodological support for the strength design and optimization of casing systems under volume fracturing conditions.

4 Analysis of Non-Uniform Load Outside Casing during Horizontal Well Volume Fracturing

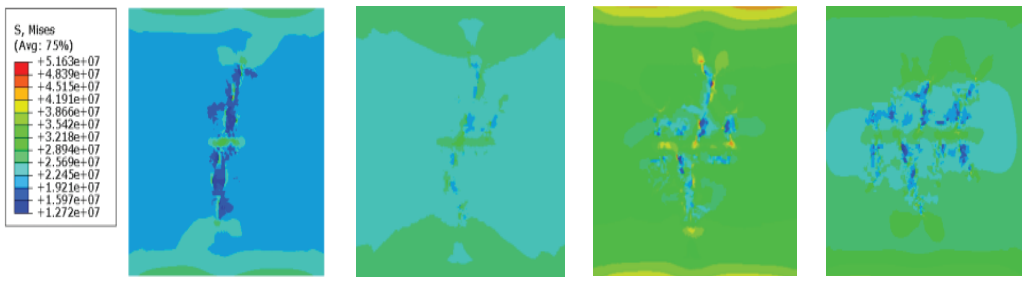
During horizontal well volume fracturing, parameters such as cluster spacing, horizontal *in-situ* stress anisotropy, formation elastic modulus, and fluid injection rate exert significant influence on the initiation and propagation of complex fractures in the near-wellbore region. To illustrate this, a representative horizontal well from the Daqing Oilfield is selected as the case study, and the fundamental well parameters are summarized in Table 2.

Taking different spacing as an example to analyze the calculation results, when the horizontal geostress difference is 5 MPa, the formation elastic modulus is 25 GPa, and the single cluster injection flow is 1.2 m^3/min, the changes of formation parameters after fracturing are discussed respectively when the cluster spacing is 5, 10, 15, and 20 m. Fig. 7 illustrates the variation characteristics of formation stress and the evolution of fracture extension under compressive conditions; Fig. 8 presents the redistribution of the *in-situ* stress field following volume fracturing; Fig. 9 depicts the magnitude of *in-situ* stress in the formation extracted along the casing.



(**a**) gap 5 m (**b**) gap 10 m (**c**) gap 15 m (**d**) gap 15 m

Figure 7: Comparison of fracture propagation rules after volume fracturing.



(**a**) gap 5 m (**b**) gap 10 m (**c**) gap 15 m (**d**) gap 15 m

Figure 8: Comparison of *in-situ* stress field variations following volume fracturing.

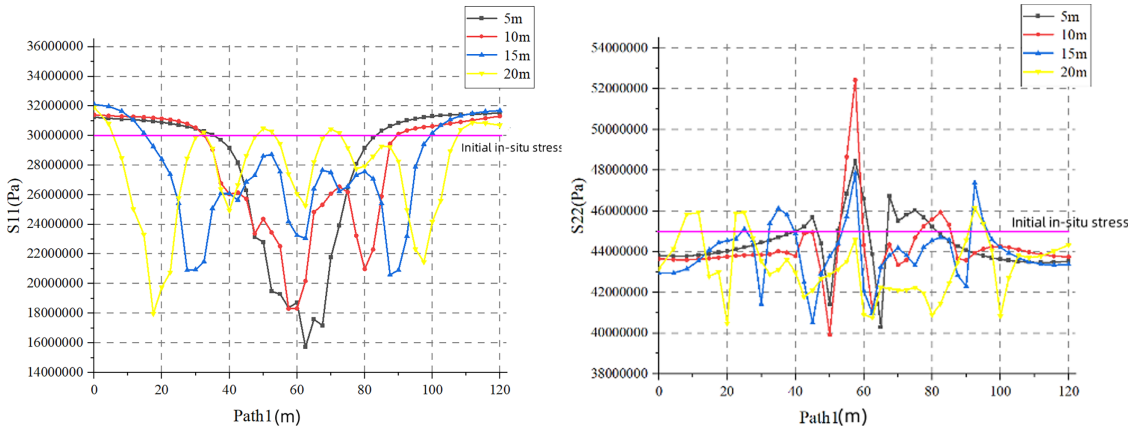


Figure 9: Comparison of *in-situ* stress changes after fracturing along the casing reservoir.

From the calculated near-wellbore formation stress distribution, it is observed that the *in-situ* stress magnitude decreases noticeably at the perforation location. This phenomenon arises because the far-wellbore formation undergoes structural damage during the fracturing stage, leading to the occurrence of a "stress deficit." Such a deficit reduces the confinement capacity of the surrounding rock and consequently lowers the pressure acting on the near-wellbore region, thereby altering its stress state. Furthermore, owing to the non-uniform expansion of induced fractures throughout the fracturing process, the restraining effect exerted by the far-wellbore formation on the near-wellbore zone is not weakened uniformly. This asymmetry manifests

along both axial and radial directions of the wellbore and ultimately results in a heterogeneous distribution of *in-situ* stress within the near-wellbore formation.

As illustrated in Fig. 9, when the cluster spacing increases, the numerical fluctuation of *in-situ* stress component S11 along the X-axis direction exhibits the largest variation, with the fluctuation magnitude decreasing from 11.9 to 6 MPa, corresponding to a reduction of 5.9 MPa. Moreover, the *in-situ* stress demonstrates a periodic variation in the X-axis direction under the influence of fracture propagation, whereas the fluctuation of stress component S22 in the Y-axis direction is the smallest, declining from 4.8 to 3.7 MPa with a reduction of 1.1 MPa. The amplitude of the *in-situ* stress difference increases progressively with cluster spacing, ranging from 5 to 7.25 MPa. These results indicate that volume fracturing intensifies the heterogeneity of the initial *in-situ* stress field, enlarges the magnitude of stress difference, and consequently promotes shear failure of natural fractures. This process further induces non-uniform deformation of the reservoir rock mass and generates uneven load distribution on the outer surface of the casing.

Following a similar analytical approach, the distribution characteristics of non-uniform load are investigated under different *in-situ* stress differences, elastic moduli, and injection displacements. The variation of initial *in-situ* stress after fracturing is examined when the *in-situ* stress difference is set to 0, 5, 10, and 15 MPa; when the formation elastic modulus is 10, 15, 20, and 25 GPa; and when the injection flow rate is 0.6, 0.8, 1.0, and 1.2 m^3/min. For comparison, no quantization procedure is applied, and Fig. 10 presents the contrast of incremental changes in *in-situ* stress difference under these various conditions. In Fig. 10, Data Point 1 corresponds to a horizontal stress difference of 0 MPa, an elastic modulus of 10 GPa, and an injection rate of 0.6 m^3/min. Data Point 2 represents 5 MPa, 15 GPa, and 0.8 m^3/min, respectively; Data Point 3 corresponds to 10 MPa, 20 GPa, and 1.0 m^3/min; and Data Point 4 represents 15 MPa, 25 GPa, and 1.2 m^3/min.

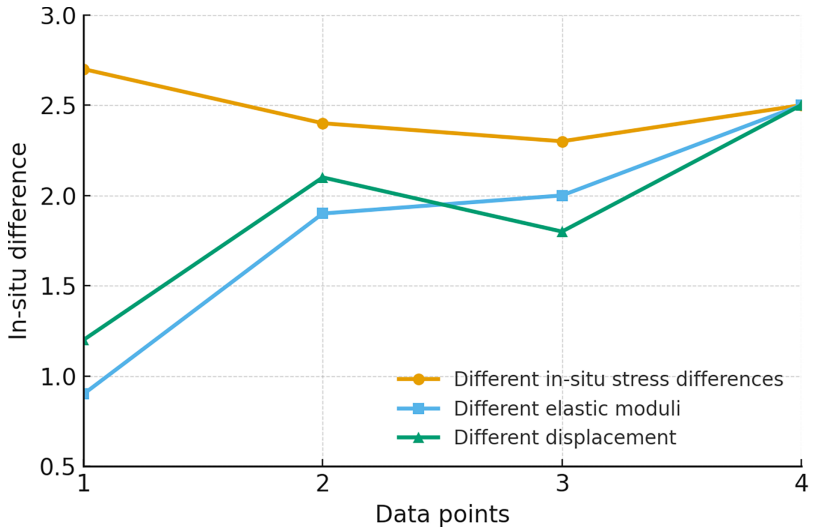


Figure 10: Comparison of *in-situ* stress differential increment under varying conditions.

As illustrated in Fig. 10, the variation in *in-situ* stress increment remains relatively small when subjected to different *in-situ* stress difference values. As the *in-situ* stress difference increases, the increment of *in-situ* stress gradually declines, with a reduction amplitude of about 0.2 MPa, suggesting that the degree of non-uniformity in stress distribution caused by stress differences during fracturing does not significantly increase. However, changes in elastic modulus and injection displacement exert a substantial influence on the magnitude of the stress difference. With higher elastic modulus and larger displacement, the increase in *in-situ* stress difference becomes more pronounced, with an amplitude ranging between 1.3 and 1.6 MPa.

This indicates that both parameters considerably amplify formation non-uniformity. A greater increase in stress difference leads to higher degrees of uneven stress distribution and consequently intensifies the non-uniform load exerted outside the casing. Therefore, from the standpoint of maintaining formation stability, adopting large-spacing and low-displacement fracturing under conditions of low elastic modulus can effectively restrain the growth of *in-situ* stress difference and contribute to stabilizing the formation.

5 Design Modification of Casing Selection for Horizontal Wells.

5.1 Casing Deformation Analysis under Non-Uniform Loading

To examine casing damage resulting from formation deformation after reservoir fracturing, the calculated non-uniform displacement outside the casing is applied as an external displacement load, while the injection pressure following hydraulic fracturing is considered as the internal load. A mechanical model for casing deformation, illustrated in Fig. 11, is constructed to evaluate the deformation response of the casing under combined internal and external loading. The total model length is 120 m, the casing outer diameter is 139.7 mm, and the wall thickness is 10.54 mm. Regarding material parameters, the casing steel type is P110, with an elastic modulus of 210 GPa, a Poisson's ratio of 0.3, and a yield strength of 758 MPa. For boundary conditions, normal constraints are applied to both ends of the model along the z-axis. The pressure exerted on the inner wall of the casing is set to 83 MPa. Incorporating the previously obtained displacement curve, the displacement values corresponding to each position are imposed symmetrically on both sides of the casing as external loading. The model is uniformly discretized using C3D8R elements.

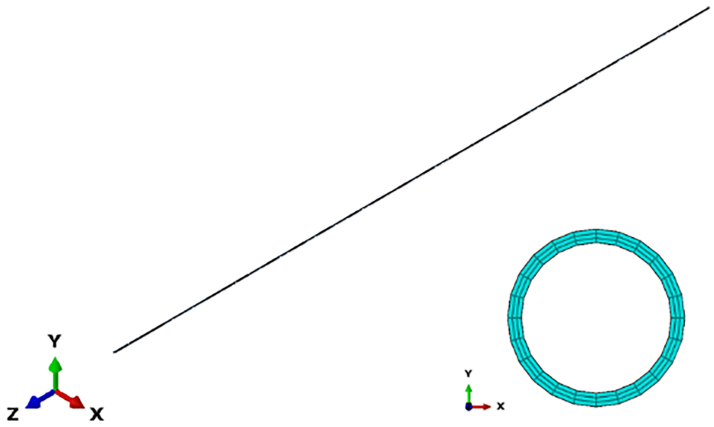


Figure 11: Casing deformation analysis model.

The deformation stress and displacement cloud maps of casing with different cluster spacing, different *in-situ* stress difference, different elastic modulus and different displacement were calculated. Fig. 12 shows the local deformation map of the most dangerous section of casing under different spacing, and Fig. 13 shows the comparison of deformation maps of the most dangerous section of casing under different conditions. In this study, the casing strength calculation is based on *API 5C3*, which assumes an axisymmetric and uniformly distributed external load. However, this assumption does not adequately capture the nonuniform stress characteristics induced by volume fracturing. To address this limitation, a correction was introduced by incorporating the nonuniform formation stress distribution obtained from the global model. The stress variation along the wellbore was converted into an equivalent external load coefficient and integrated into the external pressure term of the API formulation. This modification accounts for local stress concentration

effects and provides a more accurate representation of the actual loading conditions on the casing during fracturing operations.

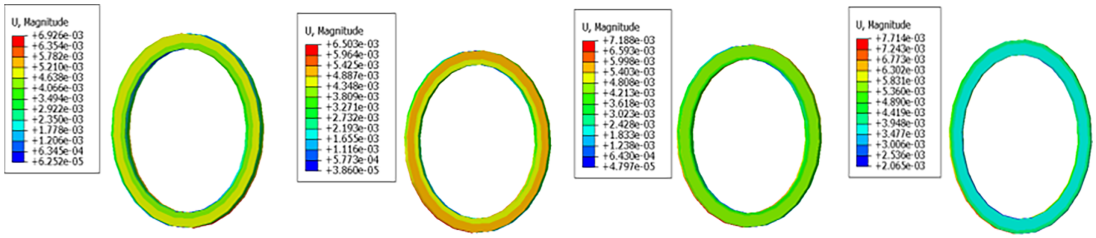


Figure 12: Comparison of deformation maps of dangerous section under different spacing.

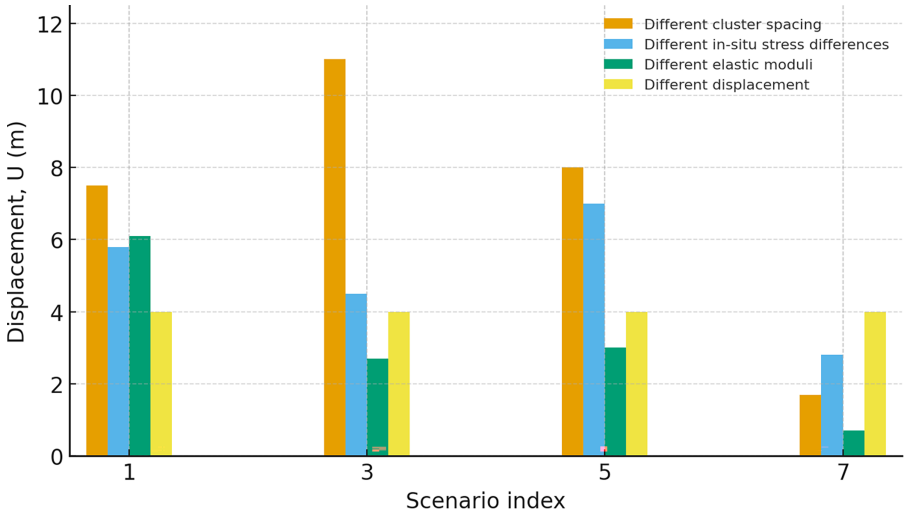


Figure 13: Minimum casing diameter changes before and after fracturing under different conditions.

When internal pressure and non-uniform displacement loading are imposed on the casing model, the overall force distribution of the casing becomes non-uniform, and stress concentration develops along the inner wall. This outcome demonstrates that fracturing injection pressure exerts a significant effect on casing stress during the fracturing process. From the comparative analysis in Fig. 13, it is evident that the formation of complex fractures leads to noticeable casing damage, while the influence of injection flow on deformation is relatively minor. By contrast, factors such as fracture aperture, *in-situ* stress difference, and formation elastic modulus exert substantial impacts, with casing deformation being more pronounced under conditions of small fracture spacing, low *in-situ* stress difference, and reduced elastic modulus. Therefore, the combined effects of these parameters on casing strength should be carefully considered when determining the internal pressure resistance of the casing.

5.2 Analysis of Casing Bearing Internal Pressure

By combining the casing deformation analysis model in Fig. 11, the change law of casing internal pressure strength when different internal pressure is applied to the inner wall of the casing under the condition of keeping the corresponding non-uniform displacement load and the three direction force unchanged, and the influence of the perforation section casing under different cluster spacing, horizontal stress difference,

formation elastic modulus and injection flow on casing internal pressure strength is analyzed. It provides theoretical support for engineering design.

When the cluster spacing is 5, 10, and 15 m, as shown in Fig. 14, the maximum equivalent stress in the casing exhibits a nearly linear increase as the spacing enlarges, with the internal pressure maintained at 90 MPa. At cluster spacings of 5 and 10 m, the maximum effective stress within the casing approaches the yield strength. However, when the spacing expands to 20 m under the same internal pressure, the maximum equivalent stress in the casing is slightly lower than that at 15 m, with the difference remaining relatively small. Therefore, to ensure casing integrity, it is advisable to adopt a cluster spacing greater than 15 m. Such an arrangement enhances the internal pressure resistance of the casing and reduces the probability of structural failure associated with yield strength exceedance.

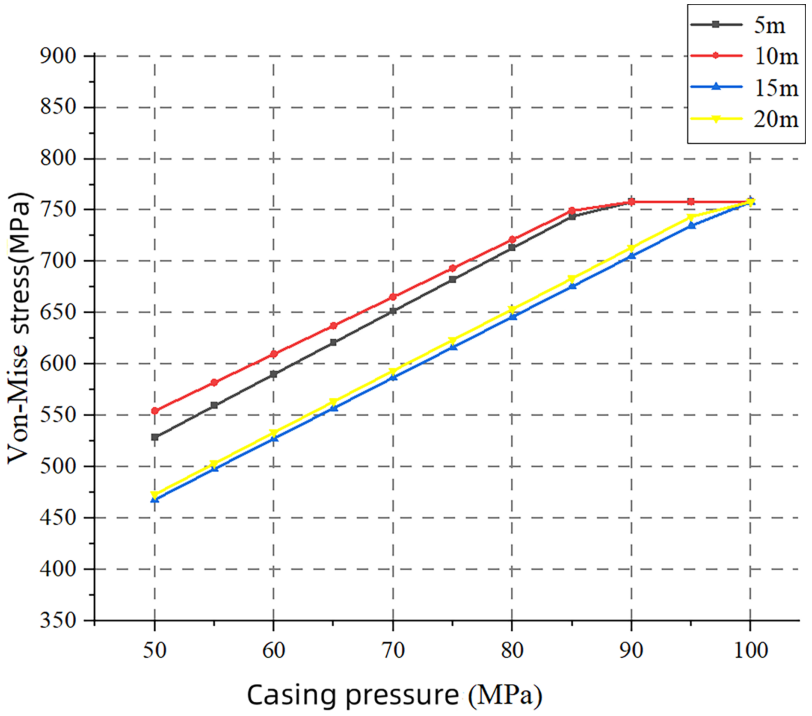


Figure 14: Variation of maximum equivalent stress of casing under different cluster spacings and internal pressures.

When the horizontal geostress difference is 0, 5, and 10 MPa, as shown in Fig. 15, the maximum equivalent stress within the casing increases approximately linearly with the growth of the geostress difference. However, when the horizontal geostress difference reaches 15 MPa under the same internal pressure, the maximum equivalent stress of the casing becomes lower than that corresponding to 10 MPa, with its value being close to the case of 5 MPa. When the internal pressure acting on the casing is 85 MPa and the horizontal geostress difference is 10 MPa, the maximum equivalent stress attains the yield strength, whereas when the horizontal geostress difference is 5 MPa, the casing does not yield until the internal pressure reaches 95 MPa. These results indicate that, within the range of 0–10 MPa, an increase in horizontal geostress difference enhances the casing's resistance to internal pressure and reduces the likelihood of failure relative to the yield strength. Conversely, in the range of 10–15 MPa, a further increase in horizontal geostress difference weakens the internal pressure resistance of the casing and raises the probability of structural failure.

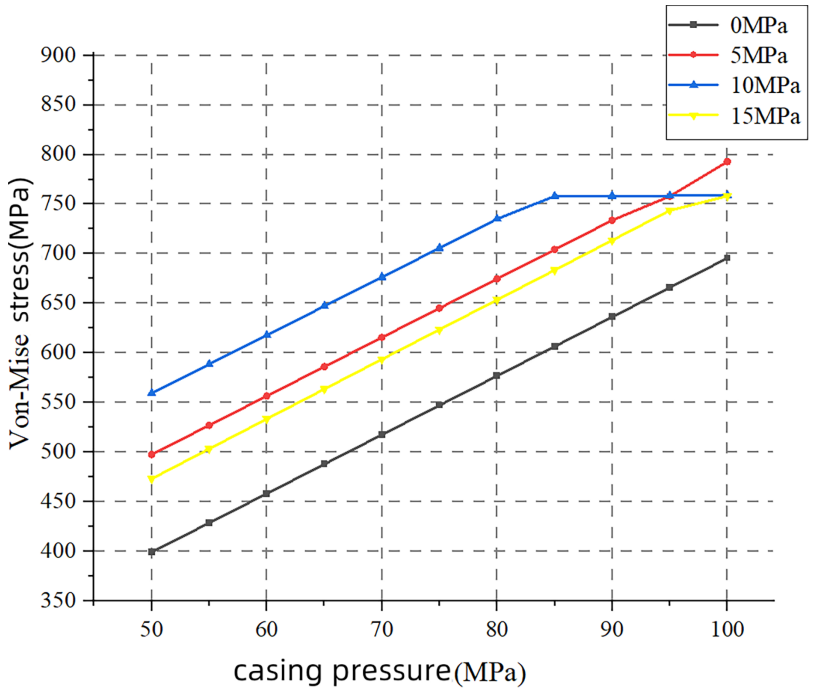


Figure 15: Variation of maximum equivalent stress of casing under different horizontal geostress differences and internal pressures.

When the formation elastic modulus is 10, 15, and 20 GPa, as shown in Fig. 16, the maximum equivalent stress in the casing increases almost linearly with the rise in elastic modulus. However, when the elastic modulus reaches 25 GPa under the same internal pressure, the maximum equivalent stress of the casing becomes slightly higher than that corresponding to 20 GPa. At an internal pressure of 55 MPa and an elastic modulus of 10 GPa, the maximum equivalent stress of the casing attains the yield strength, whereas when the elastic modulus is 15 GPa, yielding occurs only when the internal pressure reaches 80 MPa. These results demonstrate that within the elastic modulus range of 10–20 GPa, an increase in modulus enhances the casing's resistance to internal pressure and lowers the probability of casing failure relative to the yield strength. In contrast, when the modulus is between 20–25 GPa, a further increase in elastic modulus reduces the casing's internal pressure capacity and consequently increases the risk of casing failure.

When the injection flow rate is 0.6, 0.8, and 1.0 m^3/min, as shown in Fig. 17, the maximum equivalent stress in the casing exhibits a nearly linear increase with rising flow rate. However, at an injection rate of 1.2 m^3/min under the same internal pressure, the maximum equivalent stress of the casing is slightly lower than that corresponding to 1.0 m^3/min. Overall, the variation in maximum equivalent stress remains relatively small within the injection flow range of 0.8–1.2 m^3/min. When the internal pressure is 100 MPa and the injection flow is 0.8, 1.0, and 1.2 m^3/min, the maximum equivalent stress of the casing approaches the yield strength. These findings indicate that, within the injection flow interval of 0.6–1.2 m^3/min, higher injection rates enhance the casing's resistance to internal pressure and correspondingly lower the probability of casing failure relative to the yield strength.

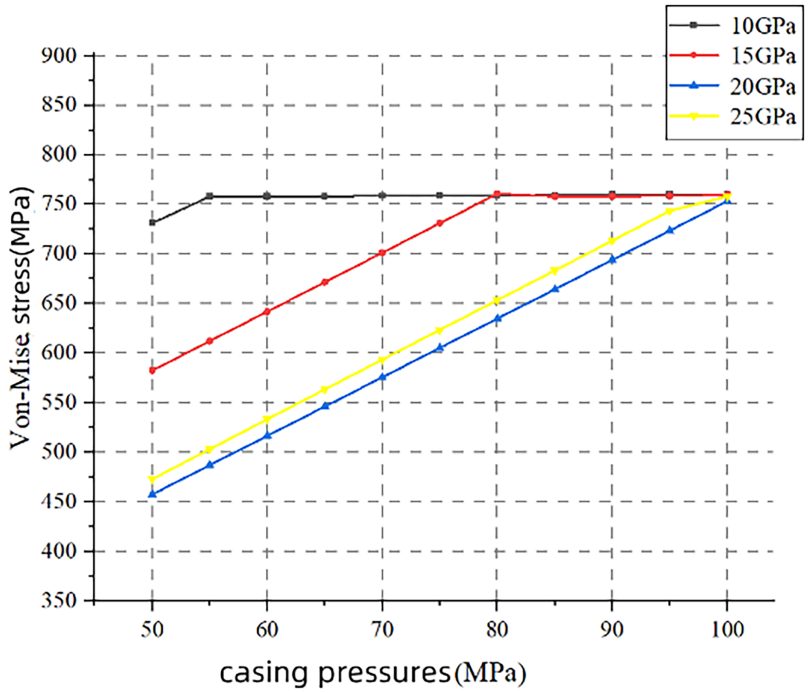


Figure 16: Variation of maximum equivalent stress of casing with formation elastic modulus under different internal pressures.

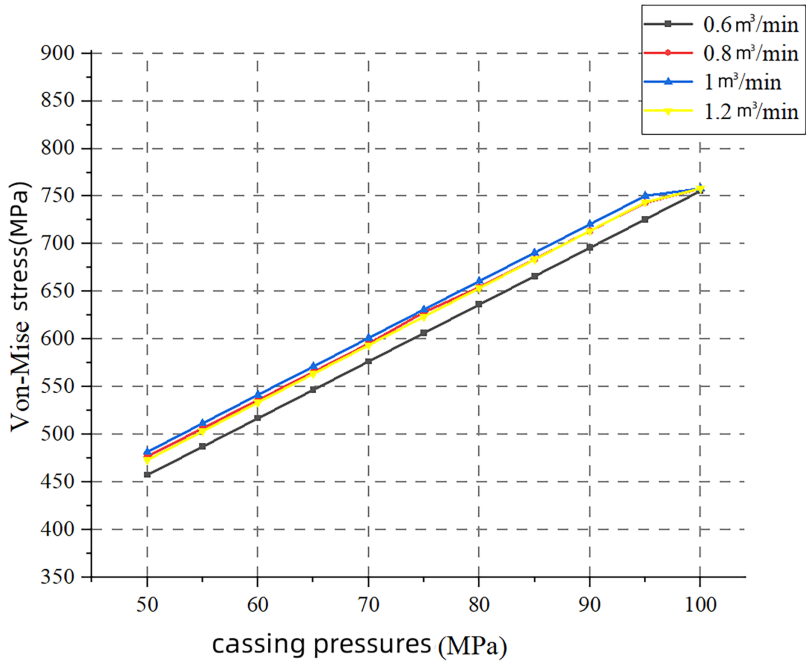


Figure 17: Variation of maximum equivalent stress of casing under different injection.

6 Conclusion

This study presents a comprehensive numerical investigation into casing deformation and failure mechanisms during hydraulic fracturing in shale horizontal wells. By integrating hydro-mechanical coupling theory, fracture mechanics, and secondary finite element development, a fully embedded fluid–solid–damage coupled model was established to reveal stress redistribution and its impact on casing integrity. The main conclusions are as follows:

(1) A fully embedded hydro-mechanical fracturing model was developed through secondary development of ABAQUS. The results show that, under initially uniform formation conditions, fracturing induces significant nonuniformity in near-wellbore stress and displacement fields, regardless of the presence of formation slip. Sensitivity analyses indicate that cluster spacing, horizontal stress difference, elastic modulus, injection rate, and slip angle strongly influence the stress redistribution, collectively increasing the likelihood of casing deformation during volume fracturing.

(2) A local strength analysis model for the formation-cement-casing system was established based on the fracturing simulation results. Nonuniform displacement loading was applied to simulate the fracturing effects. The results indicate that complex fracture development causes varying degrees of casing damage. Injection rate has a relatively minor effect, whereas fracture spacing, horizontal stress contrast, and formation stiffness play dominant roles. Smaller spacing, lower modulus, and lower stress contrast result in more pronounced casing deformation.

(3) The findings provide practical guidance for casing design and fracturing operations under volume fracturing conditions. When cluster spacing is less than 10 m, the formation modulus is below 20 GPa, or the horizontal stress contrast is high, near-wellbore stresses become strongly nonuniform, significantly increasing the risk of casing deformation. To mitigate this risk, it is recommended to increase cluster spacing (preferably >15 m), limit injection rate (<1.0 m^3/min), and use high-strength or thick-walled casing. Integrating stress monitoring with optimized fracturing parameters can further enhance well integrity and operational safety. Future work will incorporate formation heterogeneity, long-term fracture-casing coupling, and field data validation to improve the model's applicability and predictive capability.

Acknowledgement: Not applicable.

Funding Statement: This work was sponsored by the Youth Fund Project of the National Natural Science Foundation of China (No. 52404027), the General Program of the National Natural Science Foundation of China (No. 52274036) and the Postdoctoral fund of Heilongjiang Province (LBH-Z24098), CNPC Innovation Found (2024DQ02-0128), the Joint Key Project of the National Natural Science Foundation (No. U24B2034).

Author Contributions: Study conception and design: Xianan Miao, Kangxing Dong; data collection: Jinbo Li; analysis and interpretation of results: Xianan Miao, Kangxing Dong; draft manuscript preparation: Delong Yu, Zhihui Ren. All authors reviewed and approved the final version of the manuscript.

Availability of Data and Materials: Data available on request from the authors.The data that support the findings of this study are available from the corresponding author upon reasonable request.

Ethics Approval: Not applicable.

Conflicts of Interest: The authors declare no conflicts of interest.

References

1. Gao D, Xian B, Bi Y. Integrated design and control technology of liner completion and drilling for horizontal wells. Petrol Explor Dev. 2024;51(4):1009–21. doi:10.1016/s1876-3804(24)60521-5.

2. Baldino S, Meng M. Critical review of wellbore ballooning and breathing literature. Geomech Energy Environ. 2021;28:100252. doi:10.1016/j.gete.2021.100252.
3. Manjunath GL, Liu Z, Jha B. Multi-stage hydraulic fracture monitoring at the lab scale. Eng Fract Mech. 2023;289:109448. doi:10.1016/j.engfracmech.2023.109448.
4. Yusuke M, Ryota G, Noriaki W, Kazumasa S, Kohei T, Rongchang Z, et al. Creating multidirectional fractures through particle jamming. Int J Rock Mech Min Sci. 2025;188:106051. doi:10.2139/ssrn.5043462.
5. Li F, Yan W, Kong X, Li J, Zhang W, Kang Z, et al. Study on multi-factor casing damage prediction method based on machine learning. Energy. 2024;296:131044. doi:10.1016/j.energy.2024.131044.
6. Adams NJ, Mitchell RF, Eustes AW, Sampaio JH, Antonio AO. A causation investigation for observed casing failures occurring during fracturing operations. In: Proceedings of the SPE Hydraulic Fracturing Technology Conference and Exhibition; 2017 Jan 24–26; The Woodlands, TX, USA. D021S005R004 p. doi:10.2118/184868-ms.
7. Wellhoefer B, Stegent N, Tunstall M, Veillette C, Frazier G. Unique solution to repair casing failure in a HP/HT wellbore allows for successful multistage stimulation treatment in an unconventional reservoir. SPE Drill Complet. 2013;28(3):237–42. doi:10.2118/162852-pa.
8. Krzaczek M, Tejchman J. Hydraulic fracturing process in rocks-small-scale simulations with a novel fully coupled DEM/CFD-based thermo-hydro-mechanical approach. Eng Fract Mech. 2023;289:109424. doi:10.1016/j.engfracmech.2023.109424.
9. Vo Thanh H, Lee KK. Application of machine learning to predict CO_2 trapping performance in deep saline aquifers. Energy. 2022;239:122457. doi:10.1016/j.energy.2021.122457.
10. Liu J, Li P, Sun Z, Lu Z, Du Z, Liang H, et al. A new method for analysis of dual pore size distributions in shale using nitrogen adsorption measurements. Fuel. 2017;210:446–54. doi:10.1016/j.fuel.2017.08.067.
11. Tagarelli V, Santaloia F, Elia G, Cotecchia F. Numerical modelling of geological processes as means for the diagnosis of ancient landslide mechanisms. Comput Geotech. 2025;184:107238. doi:10.1016/j.compgeo.2025.107238.
12. Lin B, Guo J, Liu X, Xiang J, Zhong H. Prediction of flowback ratio and production in Sichuan shale gas reservoirs and their relationships with stimulated reservoir volume. J Petrol Sci Eng. 2020;184:106529. doi:10.1016/j.petrol.2019.106529.
13. Shaygan K, Haghshenas Lari S, Mahani H, Jamshidi S. Geomechanical investigation of casing collapse using finite element modeling: the role of cement sheath integrity. Geoenergy Sci Eng. 2024;233:212579. doi:10.1016/j.geoen.2023.212579.
14. Kyriakides S, Lee LH. Buckle propagation in confined steel tubes. Int J Mech Sci. 2005;47(4–5):603–20. doi:10.1016/j.ijmecsci.2004.11.009.
15. Brilianto RM, Qi H, Kim C. A cost-efficient hybrid double envelope worm gear design for cylindrical worm gear casing. Int J Adv Manuf Technol. 2025;140(3):2211–25. doi:10.1007/s00170-025-16439-1.
16. Dashtaki BB, Lashkaripour GR, Ghafoori M, Moghaddas NH. Numerical modeling of casing collapse in Gachsaran formation in Sirri-E oilfield in Persian Gulf. J Petrol Sci Eng. 2021;196:108009. doi:10.1016/j.petrol.2020.108009.
17. Zhang X, Li J, Zhang H, Sun X, Deng T, Yao Y, et al. Casing deformation failure analysis of deep shale gas wells in Weirong block. Drill Prod Technol. 2021;44:23–7.
18. Auad IT, Yamamoto M, Carrion R. The influence of wellhead stick-up on the analysis of critical stress points on conductor casing. J Petrol Sci Eng. 2022;212:110140. doi:10.1016/j.petrol.2022.110140.
19. Wolterbeek TKT, Cornelissen EK, Nolan S, Todea F, Stam W, Roggeband SM, et al. Restoration of annular zonal isolation using localized casing expansion (LCE) technology: a proof of concept based on laboratory studies and field trial results. J Petrol Sci Eng. 2021;197:108103. doi:10.1016/j.petrol.2020.108103.
20. Eissa K, Ahmad R, Ali S. The 3D simulation of the effect of casing standoff on cement integrity by considering the direction of horizontal stresses in one of the wells of Iranian oil fields. J Pet Sci Eng. 2021;206:108980. doi:10.1016/j.petrol.2021.108980.
21. Rutqvist J, Moridis GJ, Grover T, Silpngarmlert S, Collett TS, Holdich SA. Coupled multiphase fluid flow and wellbore stability analysis associated with gas production from oceanic hydrate-bearing sediments. J Petrol Sci Eng. 2012;92–93:65–81. doi:10.1016/j.petrol.2012.06.004.

22. Rasouli V, Pallikathekathil ZJ, Mawuli E. The influence of perturbed stresses near faults on drilling strategy: a case study in Blacktip field, North Australia. J Petrol Sci Eng. 2011;76(1–2):37–50. doi:10.1016/j.petrol.2010.12.003.
23. Fan MT, Li J, Liu GH. Stress sensitivity analysis of casing in multi-stage fracturing based on step-by-step finite element method. Sci Technol Eng. 2017;17(16):50–5. (In Chinese). doi:10.22399/ijcesen.418035.
24. Kim J, Moridis GJ, Rutqvist J. Coupled flow and geomechanical analysis for gas production in the Prudhoe Bay Unit L-106 well Unit C gas hydrate deposit in Alaska. J Petrol Sci Eng. 2012;92–93:143–57. doi:10.1016/j.petrol.2012.04.012.
25. Moghadam A, Castelein K, ter Heege J, Orlic B. A study on the hydraulic aperture of microannuli at the casing-cement interface using a large-scale laboratory setup. Geomech Energy Environ. 2022;29:100269. doi:10.1016/j.gete.2021.100269.
26. Elkhoury JE, Bérard T, Desroches J, Peyret E, Prioul R, Crisci E, et al. *In situ* static elastic properties assessment and validation with pressuremeter testing using a formation tester tool. Geomech Energy Environ. 2024;40:100619. doi:10.1016/j.gete.2024.100619.
27. Hatambeigi M, Anwar I, Lord DL, Hart D, Taha MR, Stormont JC. Wellbore cement fracture permeability as a function of confining stress and pore pressure. Geomech Energy Environ. 2023;33:100428. doi:10.1016/j.gete.2022.100428.
28. Richard JD, Sam A, Robert SW, Robert BJ, Charlotte A, Fred W, et al. Oil and gas wells and their integrity: implications for shale and unconventional resource exploitation. Mar Pet Geol. 2014;56:239–54. doi:10.1016/j.marpetgeo.2014.03.001.
29. Huerta NJ, Bryant SL, Strazisar BR, Hesse M. Dynamic alteration along a fractured cement/cement interface: implications for long term leakage risk along a well with an annulus defect. Energy Proc. 2011;4:5398–405. doi:10.1016/j.egypro.2011.02.524.
30. Liu N, Wang Y. Deflection of hydraulic fractures and shear stress disturbance considering thermal effects: a numerical case study. Energies. 2022;15(13):4888. doi:10.3390/en15134888.
31. Wang X, Liu C, Wang H, Liu H, Wu H. Comparison of consecutive and alternate hydraulic fracturing in horizontal wells using XFEM-based cohesive zone method. J Petrol Sci Eng. 2016;143:14–25. doi:10.1016/j.petrol.2016.02.014.
32. Wang Y, Ju Y, Chen J, Song J. Adaptive finite element-discrete element analysis for the multistage supercritical CO_2 fracturing and microseismic modelling of horizontal wells in tight reservoirs considering pre-existing fractures and thermal-hydro-mechanical coupling. J Nat Gas Sci Eng. 2019;61:251–69. doi:10.1016/j.jngse.2018.11.022.
33. Hampton JC, Boitnott GN. The misnomer of effective stress and its relation to biot coefficients. In: Proceedings of the 52nd US Rock Mechanics/Geomechanics Symposium; 2018 Jul 17–20; Seattle, WA, USA. p. ARMA-2018-1130.
34. Kohl T, Evansi KF, Hopkirk RJ, Rybach L. Coupled hydraulic, thermal and mechanical considerations for the simulation of hot dry rock reservoirs. Geothermics. 1995;24(3):345–59. doi:10.1016/0375-6505(95)00013-g.
35. Liu X, Rasouli V, Guo T, Qu Z, Sun Y, Damjanac B. Numerical simulation of stress shadow in multiple cluster hydraulic fracturing in horizontal wells based on lattice modelling. Eng Fract Mech. 2020;238:107278. doi:10.1016/j.engfracmech.2020.107278.